J Mater Sci (2018) 53:9411–9428

Ceramics

Micro-CT-based identification of double porosity in fired clay ceramics

Hawraa Kariem[1], Christian Hellmich[1,*], Thomas Kiefer[1], Andreas Jäger[2], and Josef Füssl[1]

[1] *Institute for Mechanics of Materials and Structures, Vienna University of Technology (TU Wien), Karlsplatz 13/202, 1040 Vienna, Austria*

[2] *Wienerberger AG, Wienerbergstraße 11, 1100 Vienna, Austria*

Received: 20 February 2018
Accepted: 28 March 2018
Published online:
5 April 2018

ABSTRACT

Optimizing thermal and mechanical properties of clay block masonry requires detailed knowledge on the microstructure of fired clays. We here identify the macro- and microporosity stemming from the use of three different pore-forming agents (expanded polystyrene, sawdust, and paper sludge) in different concentrations. Micro-CT measurements provided access to volume, shape, and orientation of macropores, and in combination with X-ray attenuation averaging and statistical analysis, also to voxel-specific microporosities. Finally, the sum of micro- and macroporosity was compared to corresponding data gained from two statistically and physically independent methods (namely from chemical analysis in combination with weighing, and from mercury intrusion porosimetry). Satisfactory agreement of all these independently gained experimental data renders our new concept for identifying the pore spaces of fired clay as a very promising tool supporting the further optimization of clay blocks.

List of symbols

a	Slope parameter
b	Intercept parameter
$\mathrm{err}^{\mathrm{CT}}$	Relative error in micro-CT-based porosity determination, with respect to weighing-based determination
$\mathrm{err}^{\mathrm{Hg-intr}}$	Relative error in mercury intrusion-based porosity determination, with respect to weighing-based determination
GV	Voxel-specific attenuation-related grey value
$\mathrm{GV}_{\mathrm{Air}}$	Attenuation-related grey value of air
$\mathrm{GV}_{\mathrm{Al}}$	Attenuation-related grey value of aluminium
$\mathrm{GV}_{\mathrm{FC}}^{\mathrm{peak}}$	The most frequently occurring grey value of the fired clay matrix domain
$\mathrm{GV}_{\mathrm{thr}}$	Grey value threshold value
$m_{\mathrm{Dilatometer+Hg+Sample}}$	Mass of dilatometer filled with mercury and sample
$m_{\mathrm{Dilatometer+Hg}}$	Mass of dilatometer filled with mercury
$m_{\mathrm{Dilatometer}}$	Mass of dilatometer

Address correspondence to E-mail: christian.hellmich@tuwien.ac.at

https://doi.org/10.1007/s10853-018-2281-9

m_{dry}	Mass of dry ceramic sample
PDF	Probability density function
V_{FC}	Volume of the fired clay matrix in ceramic sample
$V_{micropores}$	Volume of micropores in ceramic sample
V_{por}	Volume of pores in ceramic sample
V_{sample}	Volume of ceramic sample
w_i	Weight fraction of *i*th constituent of the clay matrix
w_{dry}	Weight of dry ceramic sample
w_{sample}	Weight of ceramic sample
w_{sub}	Weight of submerged ceramic sample
w_{wet}	Weight of hydrated ceramic sample
NIST	National Institute of Standards and Technology
$(\mu/\rho)_i$	X-ray mass attenuation coefficient of *i*th constituent of theoretically completely dense clay matrix
Δm	Difference in mass, between the dilatometer filled with both ceramic sample and mercury, and the solely mercury-filled dilatometer
δ	Orientation angle of macropore
ϵ	Photon energy
μ	Attenuation coefficient
μ_{Air}^{NIST}	Attenuation coefficient of air, according to the NIST database
μ_{Al}^{NIST}	Attenuation coefficient of aluminium, according to the NIST database
μ_{FC}^{peak}	Most frequently occurring attenuation coefficient in the fired clay matrix domain
μ_{Si}^{NIST}	Attenuation coefficient of a theoretically completely dense clay matrix, derived from the NIST database
ϕ	Voxel-specific microporosity
ϕ^{peak}	Most frequently occurring value of voxel-related microporosity
ϕ_{macro}	Ceramic sample-related macroporosity
ϕ_{micro}	Ceramic sample-related microporosity
$\phi_{sample}^{Hg-intr}$	Ceramic sample-related total porosity, obtained by mercury intrusion porosimetry
$\phi_{sample}^{weighing}$	Ceramic sample-related total porosity, obtained by weighing tests
ϕ_{sample}^{CT}	Ceramic sample-related total porosity, obtained from micro-CT
ρ_{sample}	Ceramic sample-related mass density
ρ_{Si}	Mass density of the theoretically completely dense clay matrix
ρ_{xylene}	Mass density of xylene

Introduction

Clay block masonry comfortably combines thermal and mechanical competences, making it one of the most sustainable and sought-after building materials, in particular when it comes to the construction of small storey houses. The recent quest to extend the applicability of this material, both in scope and volume, motivates deeper scientific scrutiny into what actually lies at the origin of the aforementioned comfortable combination of material characteristics. It is well accepted that porosities which are induced in a more or less designed way at different scales into the material, are the key governing factor for both its mechanical and thermal properties [1, 2]. In this context, pore-forming agents are used to increase porosity at scales ranging from micrometres to millimetres, in order to enhance the thermal insulation characteristics of the material. For the time being, the actual effect of this measure can only be determined empirically, through direct macroscopic testing. A first step towards a more scientific exploration of this effect is the quantification of the porosities themselves, and this is the focus of the present paper. Therefore, our preferred method of choice is micro-computed tomography, which, in recent years, has not only revealed microstructural features as represented by voxel-built patterns [3], but also basic compositional information within each and every voxel [4–6]. Accordingly, after presenting the investigated material in the "Investigated materials and micro-CT scanning" section, the "Methods for macroporosity determination" section is devoted to the determination of the ceramic macroporosity from thresholding-based image analysis, while the "Methods for microporosity determination" section describes how fundamental relations from X-ray physics, in combination with basic knowledge on fired clay chemistry, allow for the determination of the microporosity within each and every voxel. In order to check this new way of 3D quantification of the dual-scale ceramic porosities, independent experimental access to the (average) porosities is provided by mercury intrusion porosimetry and weighing tests, as described in the "Mercury intrusion porosimetry and weighing tests" section. The corresponding results are presented in the "Results and discussion" section, and discussed thereafter.

Materials and methods

Investigated materials and micro-CT scanning

Ceramic specimens with dimensions $30 \times 15 \times 125\,\text{mm}^3$ were fired at 880 °C. Their extrusion direction was parallel to the edge measuring 125 mm. These specimens exhibited different concentrations of different pore-forming agents, namely expanded polystyrene (EPS) in mass fractions of 10 and 20%, as well as paper sludge and sawdust in mass fractions of 10, 20, and 40%, respectively. For reference purposes, we also investigated ceramic samples made of pure clay without pore-forming agents, fired at 880 and 1100 °C. In order to image the ceramic microstructures by means of micro-computed tomography (μCT40, Scanco, Switzerland), ten smaller samples with dimensions $6 \times 5 \times 15\,\text{mm}^3$ were cut out from the aforementioned samples, by means of a distilled water-cooled low-speed diamond saw (Isomet, Buehler, USA). The extrusion direction of the aforementioned smaller samples was parallel to the edge measuring 6 mm. The following settings were used in the scanning process: source current 114 μA, source voltage 70 kVP, integration time 300 ms. The voxel size of the resulting micro-CT images was $6 \times 6 \times 6\,\mu\text{m}^3$, and the voxel-specific attenuation was characterized through a 16-bit grey value scale ranging from 0 to 32767.

Methods for macroporosity determination

First of all, the high-resolution micro-CT images were smoothed by means of a 3D median filter, in order to reduce ring artefacts, as it is done with various CT applications [7, 8]. Then, these cleaned image stacks were considered to illustrate two material phases at the observation scale of millimetres: (1) microporous fired clay matrix and (2) macropores. The characteristics of these two phases are quantified from normalized frequency plots (histograms) of the grey values assigned to all voxels making up the three-dimensional image stack of each and every scanned sample. Therefore, the histograms are optimally represented as the superposition of two Gaussian distribution functions, with correspondingly optimized standard deviations and expected values. The latter are denoted as GV_{air}, the most frequently occurring voxel filled by air, and GV_{FC}^{peak}, the most frequently occurring grey value filled by fired clay matrix, see Fig. 2. The optimization process is performed on the cumulative distribution function, by means of an evolutionary algorithm, as described elsewhere [9]. The intersection of the two Gaussian distribution functions serves as threshold value GV_{thr}, which discriminates macropores and fired clay matrix: all voxels with $GV > GV_{thr}$ represent fired clay matrix, and the remaining ones represent macropores. The latter can be suitably illustrated through an image segmentation process, see Fig. 1. The macropore volume fractions of the samples, ϕ_{macro}, was calculated by summing up, from 0 to GV_{thr}, the normalized frequency values of the grey value histogram, see Fig. 2c,

$$\phi_{macro} = \sum_{x=0}^{GV_{thr}} \text{PDF}(x) \times 100 \tag{1}$$

The macropores are then further analysed by ImageJ, a public-domain, Java-based image processing software developed at the National Institutes of Health [10]. Two additional plugins, 3D object counter [11] and BoneJ particle analyser [12], were used for identifying the desired geometric properties of the macropores: the 3D object counter delivered the volume and the surface of the pores. Furthermore, the Feret diameters [13] of the macropores along the x-, y-, and z-directions were determined, resulting in macropore-specific bounding boxes. In more detail, the smallest possible cuboids enclosing a

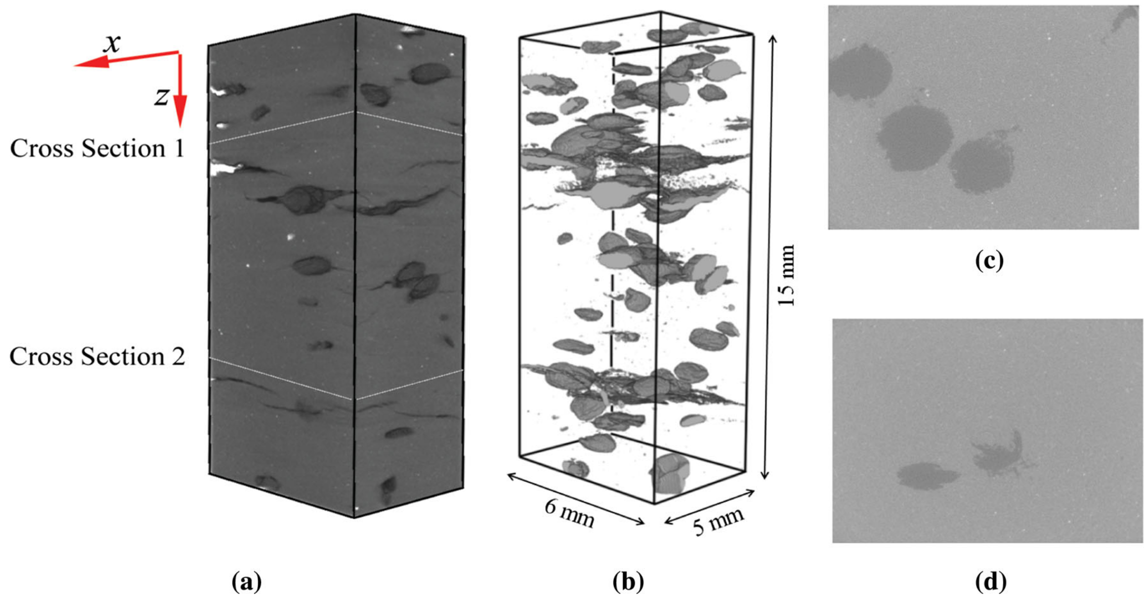

Figure 1 Micro-computed tomography of sample with 20% EPS (**a**), and segmentation-based illustration of macropores (**b**); grey value distributions throughout cross sections indicated in (**a**): cross section 1 (**c**), and cross section 2 (**d**). The x-axis indicates the extrusion direction.

pore were identified and characterized by the coordinates of their upper left corner, as well as by their widths, heights, and depths. Finally, the particle analyser gave access to the principal direction related to the largest eigenvalue I_1 of the inertia tensor of each pore [12]. The orientation of the macropore was computed in terms of the angle δ between the extrusion direction (labelled by coordinate x-direction) and the aforementioned principal direction. This allowed for comparing the orientation of the macropores between the different samples.

Methods for microporosity determination

The microporous fired clay matrix material is considered as consisting of two phases at the single micrometre scale of one scanned voxel: (1) dense aluminium silicate matrix and (2) micropores. In order to determine the microporosity inside each and every voxel, the protocol of Czenek et al. [6] was adopted to the current needs. First of all, the imaging activities described in the "Methods for macroporosity determination" section were complemented by scanning a single-crystal aluminium cylinder with a diameter of 6 mm and a height of 3 mm. The most frequently occurring grey value within this aluminium sample is denoted as GV_{Al}, and it amounted to $GV_{Al} = 10544$. This value is instrumental in assigning the attenuation-related grey values to the corresponding actual X-ray attenuation coefficients. The respective linear relation is defined by slope and intercept parameters a and b, and the latter depend on the photon energy ϵ. Mathematically, this reads as [6]

$$\mu(\epsilon) = a(\epsilon) \times \mathrm{GV} + b(\epsilon) \tag{2}$$

Strictly speaking, Eq. (2) is only valid for monochromatic X-rays as encountered with synchrotron computed tomography. However, Eq. (2) turns out as a suitable approximative description of the polychromatic case when ϵ is considered as an average photon energy, see the end of the "Results of microporosity determination" section for further discussion of this issue. Under these conditions, parameters a and b can be retrieved from X-ray physics-supported image analysis, in the line of [6]: the grey values GV_{Al} and GV_{air}, as determined in the "Methods for macroporosity determination" section, are related to the attenuation coefficients of air and aluminium, μ_{air} and μ_{Al}, which are known from the NIST database [14–16], see Fig. 3, and this provides two linear equations for the coefficients a and b, reading as

$$\mu_{Air}^{NIST}(\epsilon) = a(\epsilon) \times \mathrm{GV}_{Air} + b(\epsilon) \tag{3}$$

$$\mu_{Al}^{NIST}(\epsilon) = a(\epsilon) \times \mathrm{GV}_{Al} + b(\epsilon) \tag{4}$$

Still, a and b are functions of ϵ, as depicted in Fig. 4, and the actually used (average) energy ϵ still needs to

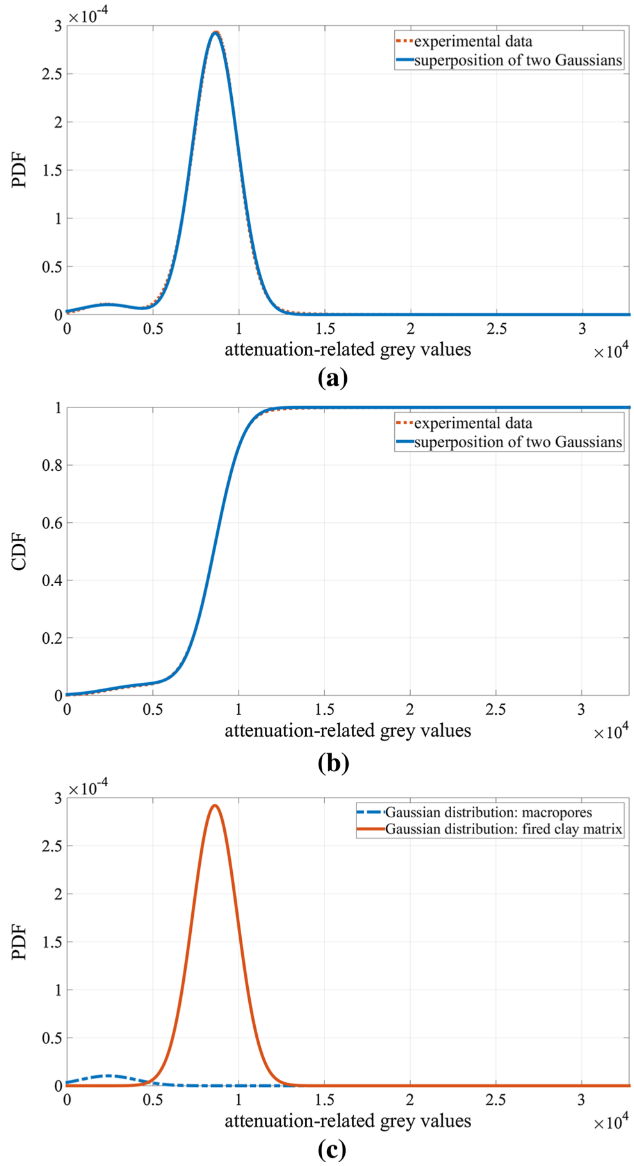

Figure 2 Statistical evaluation of voxel-specific grey values of micro-CT-scanned ceramic sample with 10% EPS: **a** normalized histogram or probability density function (PDF) of all image voxels; **b** cumulative distribution function (CDF) of all image voxels; **c** Gaussian PDFs related to macropore voxels and to fired clay matrix voxels, respectively.

be retrieved. This is done based on the grey value which most frequently occurs in the fired clay matrix, GV_{FC}^{peak}, as described in the "Methods for macroporosity determination" section, and on the corresponding peak attenuation coefficient μ_{FC}^{peak}, which according to Eq. (2), are related to each other through

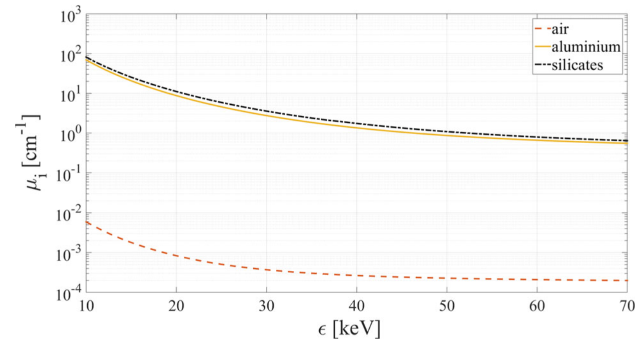

Figure 3 X-ray attenuation coefficients of air, aluminium, and the solid fired clay matrix consisting almost exclusively of silicates, as functions of the photon energy ϵ, according to NIST [16].

$$\mu_{FC}^{peak} = a(\epsilon) \times GV_{FC}^{peak} + b(\epsilon) \tag{5}$$

There is an independent alternative access to μ_{FC}^{peak}, via the volume average rule for attenuation coefficients, reading as [4, 17, 18]

$$\mu_{FC}^{peak} = \phi^{peak}\mu_{air} + \left(1 - \phi^{peak}\right)\mu_{Si}^{NIST} \tag{6}$$

with ϕ^{peak} as the most frequently occurring value for the microporosity, and μ_{Si}^{NIST} as the attenuation coefficient of a theoretically completely dense clay matrix. The latter consists almost exclusively of silicates, as revealed from standard X-ray fluorescence spectroscopy, see Table 1 for the chemical composition. This composition, together with the NIST database [16], provides μ_{Si}^{NIST}, see dash-dotted line in Fig. 3. In more detail, the attenuation coefficient μ_{Si}^{NIST} was computed from the X-ray mass attenuation coefficient of each molecular constituent $(\mu/\rho)_i$ and its weight fraction w_i [19], see Table 1,

$$\mu_{Si}^{NIST} = \sum_i w_i(\mu/\rho)_i \times \rho_{Si} \tag{7}$$

with $\rho_{Si} = 2.7\,g/cm^3$ being the density of the theoretically completely dense clay matrix.

The aforementioned density was determined by means of Archimedes' principle [20]. A sample fired at 880 °C without pore-forming agent was weighed, which delivered its dry weight, $w_{dry} = 7.505\,mN$. Then, it was placed in a glass beaker containing liquid xylene, which subsequently filled the pores. The sample was weighed every 4 h for 36 h. After 24 h the weight of the fully saturated sample, $w_{wet} = 8.923\,mN$, did not change any more, indicating that the sample was completely hydrated and that all the pores were filled with xylene. The hydrated

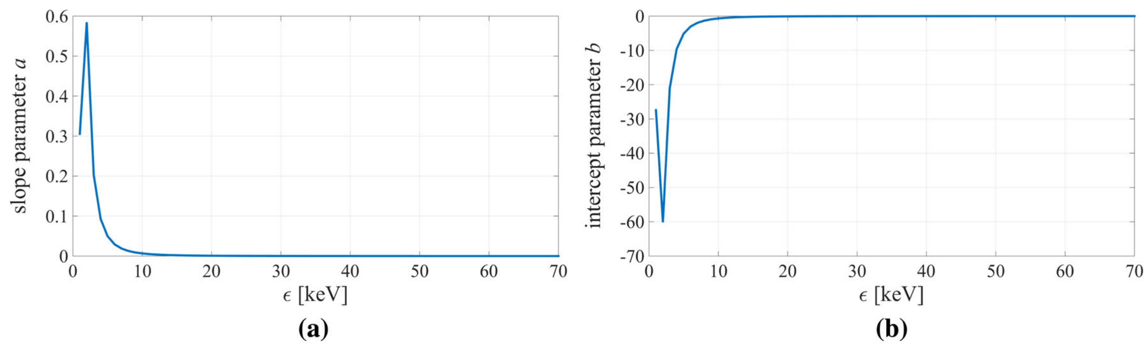

Figure 4 Slope and intercept parameters **a** and **b**, as functions of the photon energy ϵ, related to the image stack of ceramic sample with 10% EPS.

Table 1 Chemical composition of clay: chemical elements in (mass %), and in parts per million (ppm), as a function of firing temperature, obtained from X-ray fluorescence spectroscopy

Firing temperature		880 °C	1100 °C
SiO_2	(mass %)	58.4	58.7
Al_2O_3	(mass %)	17.5	17.2
TiO_2	(mass %)	0.9	0.9
Fe_2O_3	(mass %)	7.0	7.1
CaO	(mass %)	5.7	5.8
MgO	(mass %)	5.3	5.1
K_2O	(mass %)	3.0	3.0
Na_2O	(mass %)	0.9	1.0
SO_3	(mass %)	1.4	1.3
MnO	(mass %)	0.11	0.11
P_2O_5	(mass %)	0.11	0.13
Ba	(ppm)	401	420
Co	(ppm)	31	48
Cr	(ppm)	154	162
Cu	(ppm)	38	36
Ga	(ppm)	23	27
Mo	(ppm)	4	4
NB	(ppm)	20	16
Ni	(ppm)	84	83
Pb	(ppm)	25	26
Rb	(ppm)	140	139
Sr	(ppm)	205	205
V	(ppm)	133	136
Zn	(ppm)	117	114

sample was then submerged into xylene, and the weight w_{sub} of the submerged sample was measured, $w_{sub} = 5.121\,\text{mN}$. The latter weight and the dry weight then give access to the overall sample volume as

$$V_{sample} = \frac{(w_{dry} - w_{sub})g}{\rho_{xylene}} = 0.282\,\text{cm}^3, \tag{8}$$

with $\rho_{xylene} = 0.861\,\text{g/cm}^3$ as the mass density of xylene at room temperature (20 °C) and $g = 9.81\,\text{m/s}$ as the gravitational acceleration. Thus, the density ρ_{Si} of the theoretically completely dense clay matrix can be given as

$$\rho_{Si} = \frac{m_{dry}}{V_s} = 2.707\,\text{g/cm}^3, \tag{9}$$

which is equal or close to values given elsewhere [21–23].

Equating the previously described expressions for the peak attenuation coefficient μ_{FC}^{peak}, namely Eqs. (5) and (6), yields

$$a(\epsilon) \times \text{GV}_{FC}^{peak} + b(\epsilon) = \mu_{Si}^{NIST}(1 - \phi^{peak}) + \mu_{Air}\phi^{peak} \tag{10}$$

Equation (10) constitutes a non-bijective function between ϕ^{peak} and ϵ, with the characteristic that a specific value of ϕ^{peak} is related to either none, one, or two values of the (average) photon energy ϵ. As only one (average) photon energy was used for the scanning process, the one value of ϕ_{peak} which is related to only *one* photon energy ϵ, is the only and unique physically admissible (average) energy level. This provides unique values for both ϵ and ϕ^{peak}.

Once ϵ is known, the grey values of the images can be converted into attenuation coefficients, according to Eq. (2) with the functions retrieved from Eqs. (3) and (4), as depicted in Fig. 4. Subsequently, the voxel-specific microporosity follows from the average rule (6) applied to all voxels representing fired clay matrix,

$$\phi = \frac{\mu_{FC} - \mu_{Si}^{NIST}}{\mu_{Air} - \mu_{Si}^{NIST}} \tag{11}$$

The integral of the voxel-specific microporosity over the volume of the fired clay matrix yields the microporosity volume,

$$V_{micropores} = \int_{V_{FC}} \phi(x) \mathrm{d}V, \tag{12}$$

which is used to calculate the sample-specific microporosity ϕ_{micro} as

$$\phi_{micro} = \frac{V_{micropores}}{V_{sample}} \tag{13}$$

Accordingly, the ceramic sample-related total porosity derived from micro-CT can be given as

$$\phi_{sample}^{CT} = \phi_{macro} + \phi_{micro}, \tag{14}$$

with ϕ_{macro} and ϕ_{micro} according to Eqs. (1) and (13), respectively.

Mercury intrusion porosimetry and weighing tests

The total porosity of all samples as determined from (14) was checked by two independent methods, namely mercury intrusion porosimetry and weighing tests. Mercury is a non-wetting liquid that does not spontaneously infiltrate pores, so that pore infiltration requires an external pressure. Using the system Pascal 140-240/440, POROTEC GmbH, Germany, the volume of intruded mercury was measured, as well as the applied pressure [24]. The volume of intruded mercury is equal to the pore volume V_{por} of the sample. If the mass of the sample is known, also its volume can be determined; therefore, the dilatometer is filled with mercury up to a defined volume and then weighed. Thereafter, the sample is put into the dilatometer, and the rest of the defined volume in the dilatometer is filled with mercury under vacuum. The difference in mass between the dilatometer filled by mercury only and the dilatometer filled with both the sample and mercury, is equal to the mass Δm of mercury filling the volume of the sample, which reads mathematically as

$$\Delta m = \left(m_{Dilatometer+Hg} - m_{Dilatometer}\right) - \left(m_{Dilatometer+Hg+Sample} - m_{Sample} - m_{Dilatometer}\right) \tag{15}$$

Knowing also the mass density of mercury at the measured room temperature, ρ_{Hg}, the aforementioned mass difference readily gives access to the volume of the sample [25],

$$V_{sample} = \frac{\Delta m}{\rho_{Hg}} \tag{16}$$

Finally, the porosity of the sample $\phi_{sample}^{Hg-intr}$ is obtained through

$$\phi_{sample}^{Hg-intr} = \frac{V_{por}}{V_{sample}} \tag{17}$$

At higher pressures, the compressibility of mercury was considered according to the algorithm described in [21]. Since mercury intrusion porosimetry is only capable of measuring the volume of open pores with a diameter ranging from 2 nm to 500 µm, also weighing tests were performed, in order to determine the total (potentially partially closed) porosity of the samples. Their weight, w_{sample}, was measured by means of a precision balance (PGH403-S, Mettler-Toledo International Inc., Switzerland), and the exact dimensions of the samples were extracted from the micro-CT images. Considering a cuboid shape, the volume V_{sample} was computed, which in turn provides access to the sample densities ρ_{sample},

$$\rho_{sample} = \frac{w_{sample}/g}{V_{sample}} \tag{18}$$

From the latter and the known theoretical density of the silicate matrix $\rho_{Si} = 2.7\,\mathrm{g/cm^3}$, the porosity $\phi_{sample}^{weighing}$ follows as

$$\phi_{sample}^{weighing} = 1 - \frac{\rho_{sample}}{\rho_{Si}} \tag{19}$$

The latter and $\phi_{sample}^{Hg-intr}$ are compared to the porosity resulting from the micro-CT images, ϕ_{sample}^{CT}. The relative errors, err^{CT} and $\mathrm{err}^{Hg-intr}$, are calculated on the basis of $\phi_{sample}^{weighing}$, so that

$$\mathrm{err}^{CT} = 100 \times \frac{\phi_{sample}^{CT} - \phi_{sample}^{weighing}}{\phi_{sample}^{weighing}} \tag{20}$$

$$\mathrm{err}^{Hg-intr} = 100 \times \frac{\phi_{sample}^{Hg-intr} - \phi_{sample}^{weighing}}{\phi_{sample}^{weighing}} \tag{21}$$

Results and discussion

Results of macroporosity determination

Histogram evaluations as described in the "Methods for macroporosity determination" section reveal macropores to be present in samples processed with EPS and sawdust, while samples processed with paper sludge are free of macropores, see Figs. 5, 6 and 7. In this context, sawdust induces the largest macroporosity, and the largest number of macropores according to the 3D object counter evaluation described in the "Methods for macroporosity determination" section, while EPS is remarkably less effective in its pore-forming ability (see Table 2). Moreover, the sawdust-induced pores are smaller and more homogeneously distributed than the EPS-induced pores (see Fig. 8). Generally, an increase in the pore-forming agents EPS and sawdust causes a higher macroporosity and bigger macropores in the samples. It is also interesting to regard the macropore size distribution (see Figs. 9, 10): as a rule, large macropores (with volumes exceeding 10^8 μm^3) make up most of the macropore volume, while the numbers of medium-sized macropores (with volumes ranging from 10^5 and 10^8 μm^3) and of small macropores (with volume smaller than 10^5 μm^3, but still

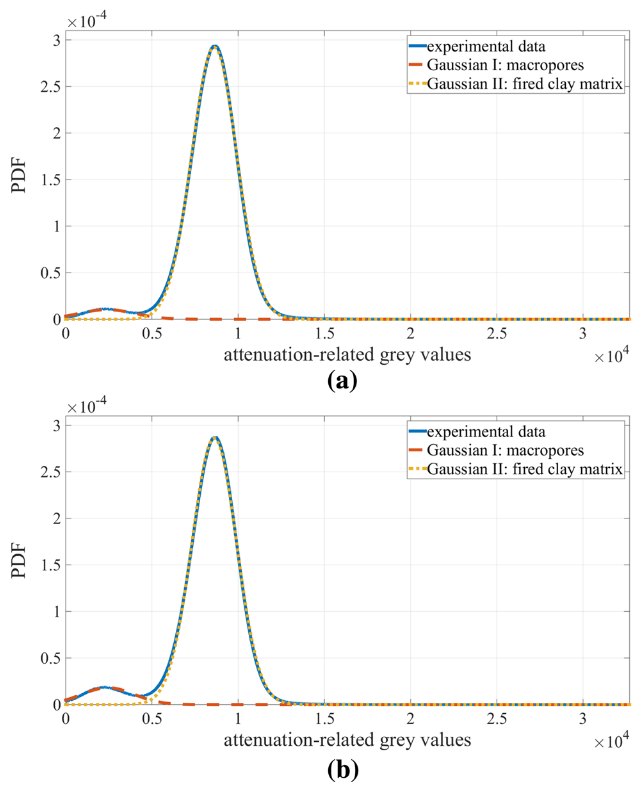

Figure 5 Probability density function (PDF) of attenuation-related grey values from micro-CT scans of samples processed with EPS: **a** 10% mass fraction, **b** 20% mass fraction; representation of experimental data through two Gaussians related to macropores and fired clay matrix, respectively.

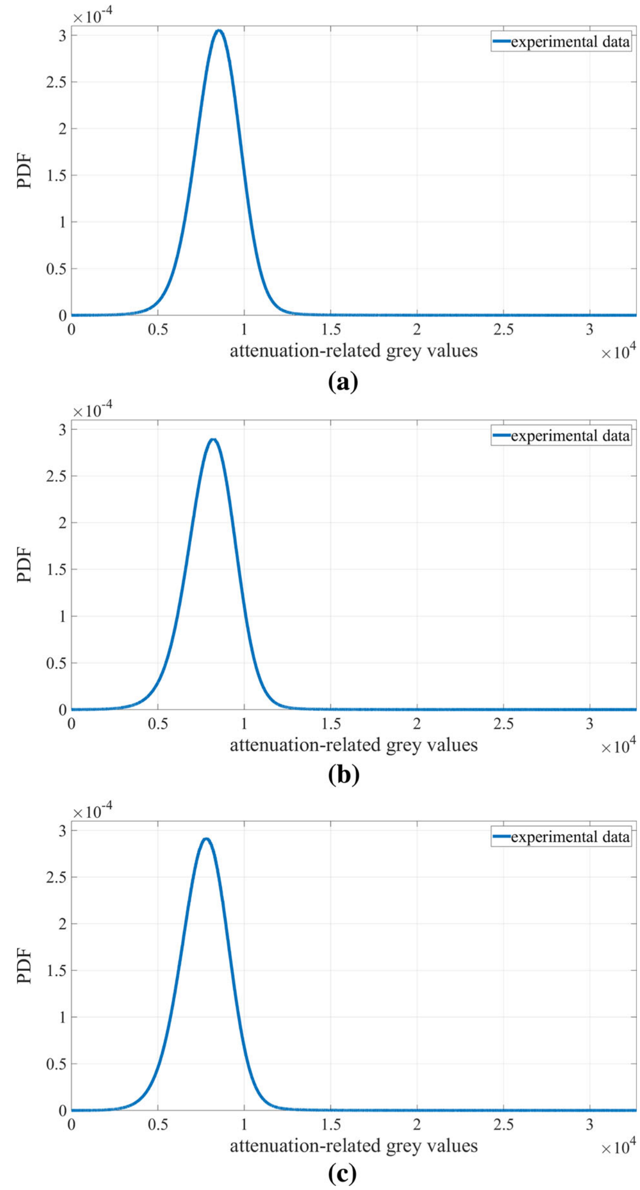

Figure 6 Probability density function (PDF) of attenuation-related grey values from micro-CT scans of samples processed with paper sludge: **a** 10% mass fraction, **b** 20% mass fraction, **c** 40% mass fraction; representation of experimental data through one Gaussian related to the fired clay matrix.

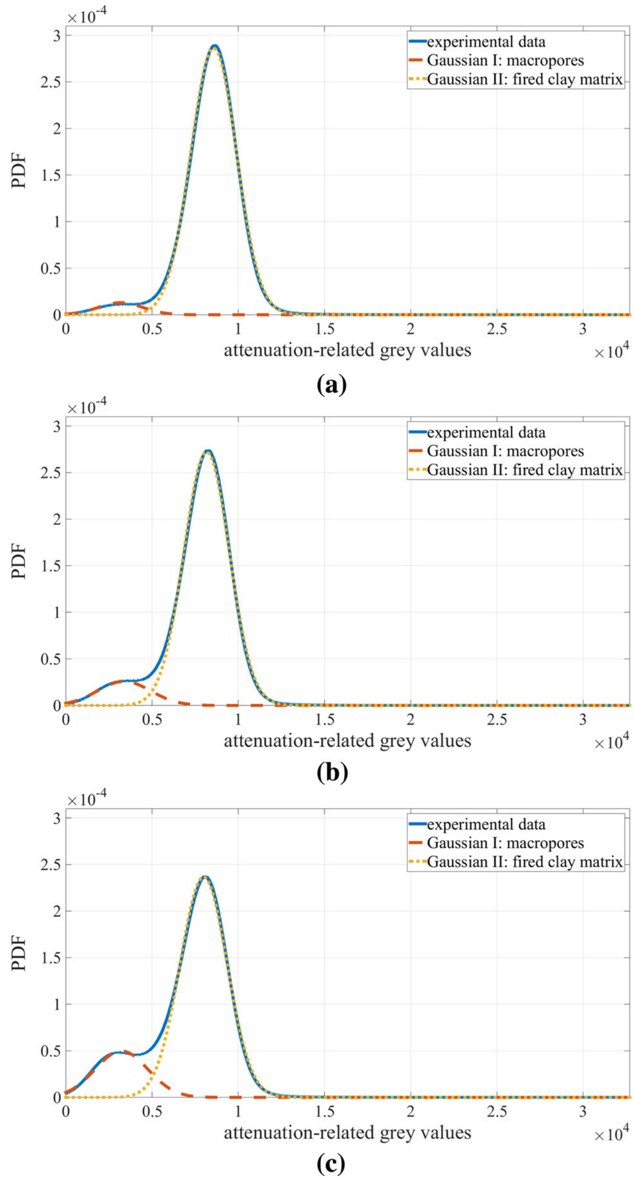

Figure 7 Probability density function (PDF) of attenuation-related grey values from micro-CT scans of samples processed with sawdust: **a** 10% mass fraction, **b** 20% mass fraction, **c** 40% mass fraction; representation of experimental data through two Gaussians related to macropores and fired clay matrix, respectively.

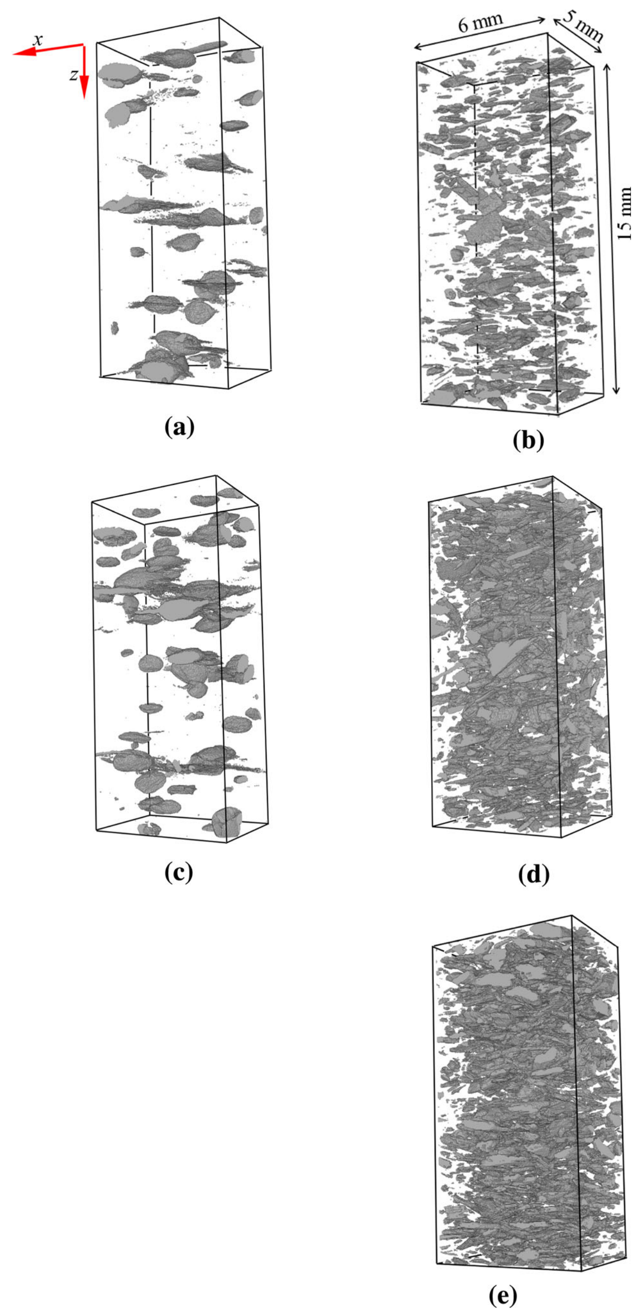

Figure 8 Segmentation-based illustration of macropores induced by pore-forming agents EPS and sawdust; extrusion direction x is illustrated in the upper left corner. **a** 10% EPS, **b** 10% sawdust, **c** 20% EPS, **d** 20% sawdust, **e** 40% sawdust.

Table 2 Characterization of the macropore space of samples with EPS and sawdust

Pore-forming agent	EPS		Sawdust		
Agent concentration (mass %)	10	20	10	20	40
Macropore volume fraction (%)	4.20	6.90	4.80	9.98	19.10
Number of macropores	2047	2496	4936	9178	6695
Volume of largest macropore (mm^3)	3.41	6.88	1.13	2.11	7.51

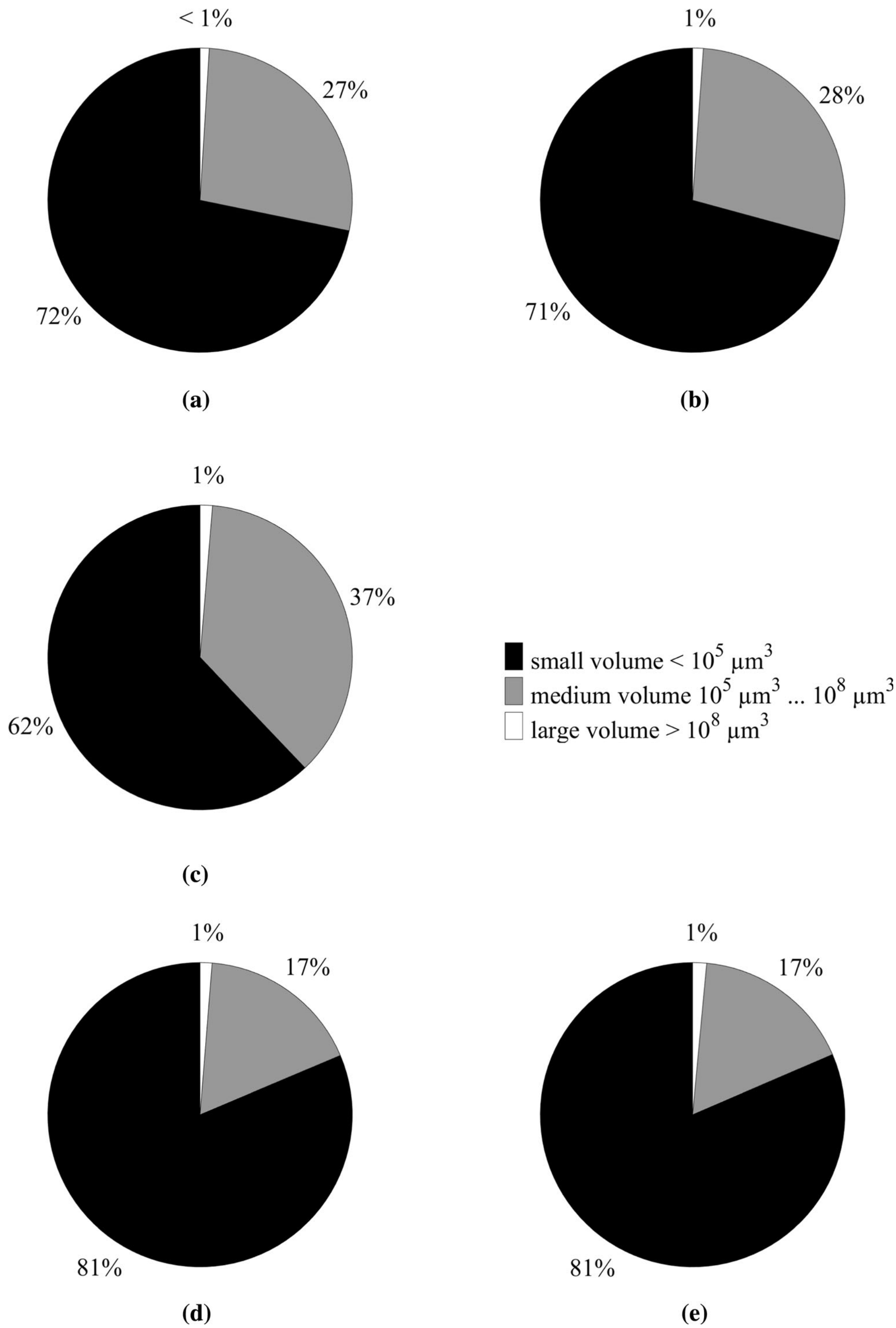

Figure 9 Frequency of macropore size categories in samples processed with sawdust at mass fractions of **a** 10%, **b** 20%, **c** 40%, and with EPS at mass fractions of **d** 10%, **e** 20%.

larger than the voxel size, with 216 μm^3) outnumber, by far, the number of the aforementioned large macropores. This effect is more pronounced with the EPS-processed samples, when compared to the sawdust-processed samples. The principal axes related to the largest eigenvalues of the pore-specific

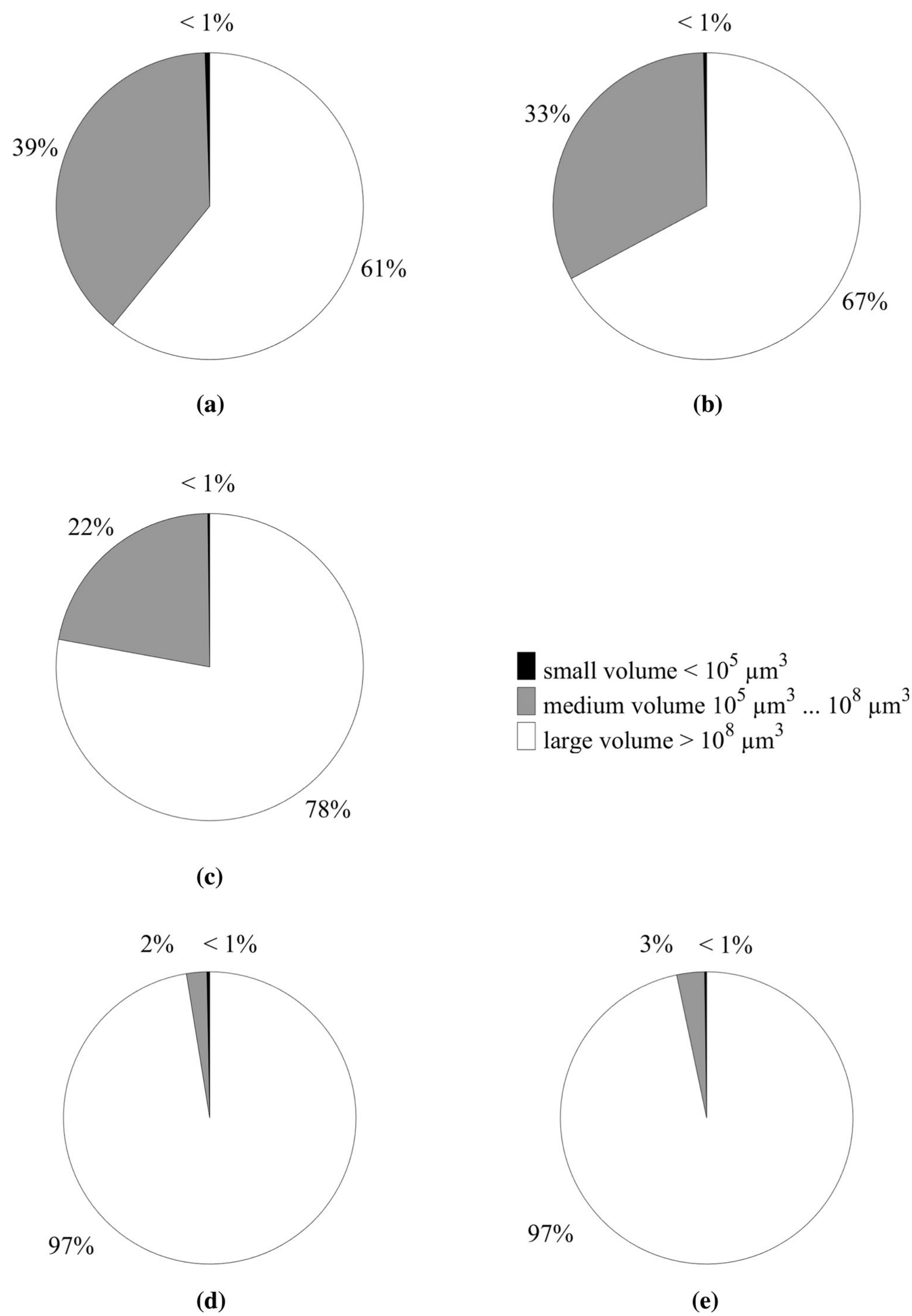

Figure 10 Volume fraction of macropore size categories in samples processed with sawdust at mass fractions of **a** 10%, **b** 20%, **c** 40%, and with EPS at mass fractions of **d** 10%, **e** 20%.

inertia tensor (quantified by the particle analyser as described in the "Methods for macroporosity determination" section) are preferentially oriented in the extrusion direction (i.e. in direction x of Fig. 8), see Fig. 11. The results of the bounding box evaluations also confirm that the macropores show a preferred orientation, as most macropores have their biggest dimension along the x-axis, the extrusion direction, see Table 3.

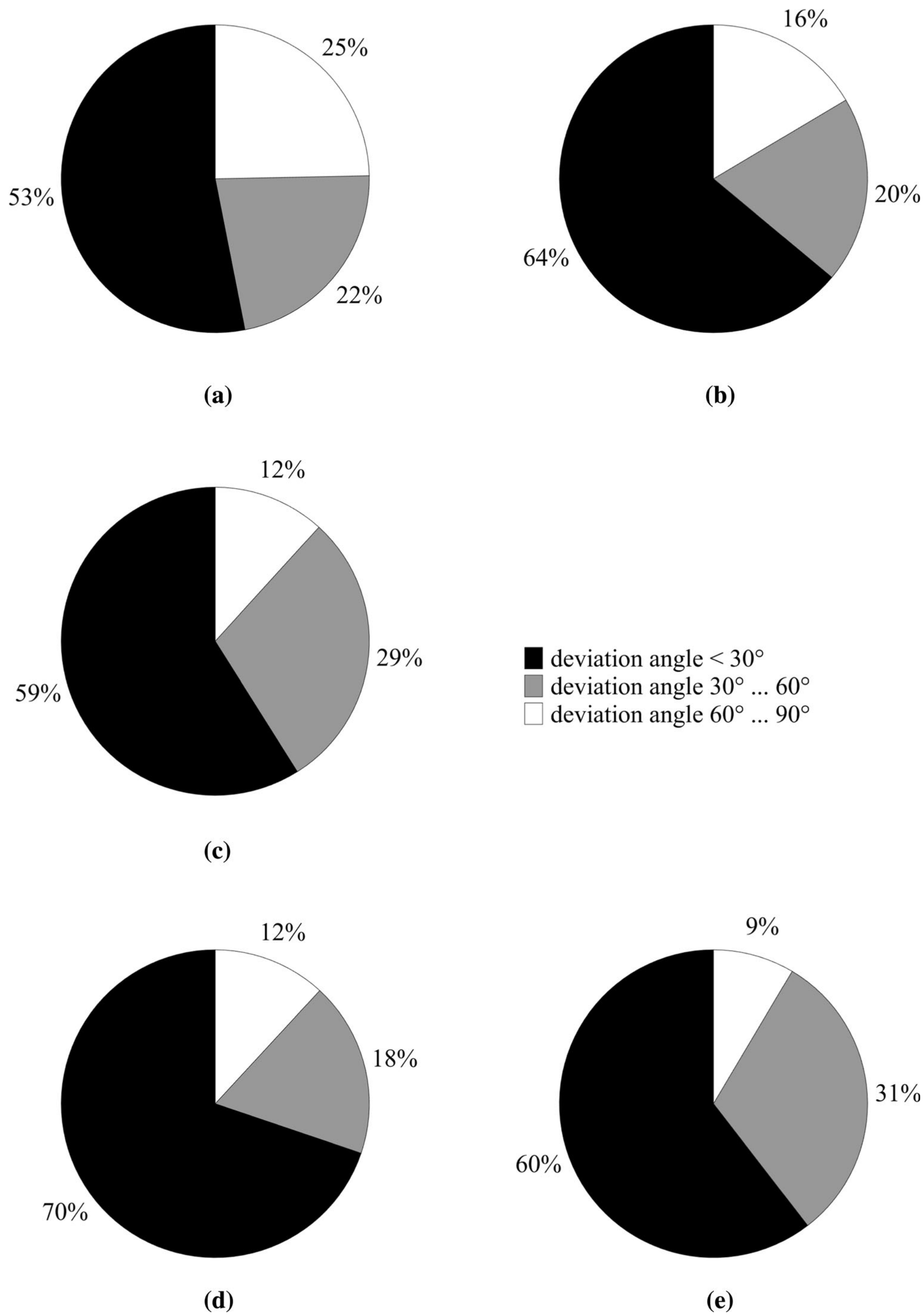

Figure 11 Volume fraction of macropore orientation categories in terms of deviation angle δ between the extrusion direction and the principal axis related to the largest eigenvalues of the macropore-specific inertia tensors; for samples processed with sawdust at mass fractions of **a** 10%, **b** 20%, **c** 40%, and with EPS at mass fractions of **d** 10%, **e** 20%.

Results of microporosity determination

Evaluation of the implicit energy–microporosity relation Eq. (10), together with the intercept and slope parameters resulting from Eqs. (3) and (4), for all samples described in the "Investigated materials and micro-CT scanning" section, yields the graphs depicted in Fig. 12. The edges in the otherwise smooth curves stem from the so-called *K*-edge of barium, known to occur at 37.4 keV [16]. The maximum values of the sample-specific graphs of Fig. 12 relate to the actual peak microporosities (as only one

Table 3 Statistical distribution of bounding box dimensions: percentage of bounding boxes with largest edges oriented in x-, y-, and z-directions

Pore-forming agent	EPS		Sawdust		
Agent concentration (mass %)	10	20	10	20	40
Percentage of bounding boxes with longest edge parallel to					
x-direction (extrusion)	51.07	45.41	62.46	61.91	67.66
y-direction	34.02	33.21	23.87	14.32	24.88
z-direction	0.62	5.84	1.86	12.40	1.17
x- and y-directions	12.53	9.46	10.02	4.28	5.62
x- and z-directions	0.62	2.46	0.63	3.85	0.27
y- and z-directions	0.38	2.03	0.48	1.71	0.21
x-, y-, and z-directions	0.76	1.59	0.69	1.53	0.19

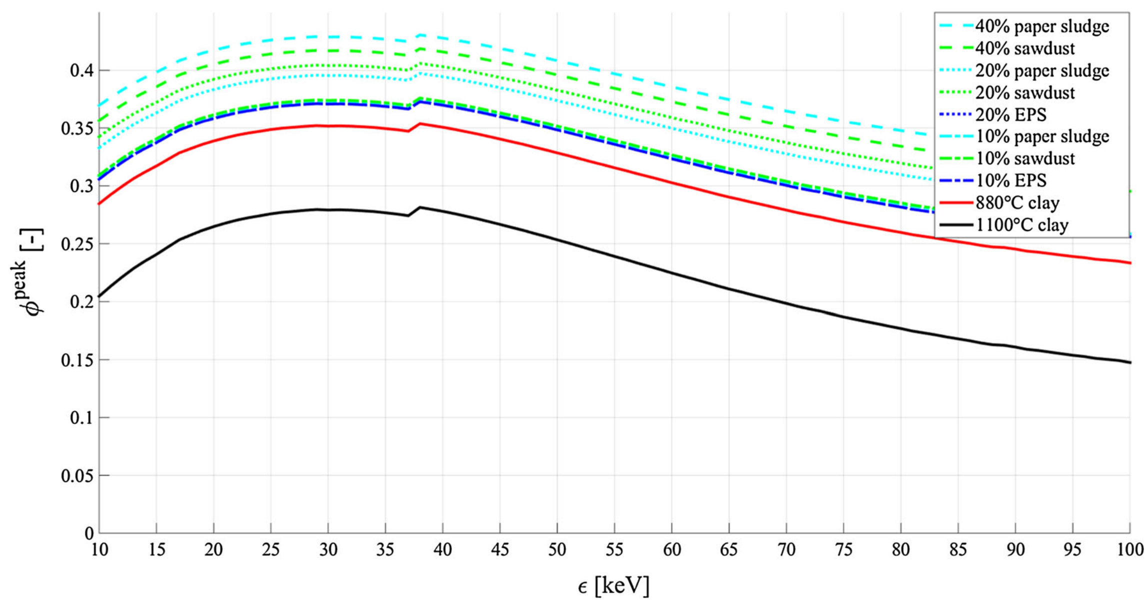

Figure 12 Voxel-related peak microporosities as a function of average photon energy according to Eq. (10): physically admissible solution at $\epsilon = 38$ keV.

Table 4 Peak microporosities ϕ^{peak} in all investigated samples

Sample characteristics	ϕ^{peak} (%)
10 (mass %) EPS; 880 °C	37.29
20 (mass %) EPS; 880 °C	37.29
10 (mass %) paper sludge; 880 °C	37.51
20 (mass %) paper sludge; 880 °C	39.74
40 (mass %) paper sludge; 880 °C	43.06
10 (mass %) sawdust; 880 °C	37.61
20 (mass %) sawdust; 880 °C	40.60
40 (mass %) sawdust; 880 °C	41.87
No agent; 880 °C clay	35.37
No agent; 1100 °C clay	28.15

average photon energy was used per scanning); these values are summarized in Table 4. The black line in Fig. 12 represents the sample without pore-forming agent fired at 1100 °C, which has expectedly the lowest microporosity since most likely the amorphous fraction of the fired clay matrix increases. Consistently, the pure clay sample fired at 880 °C, indicated by a red line in Fig. 12, has a higher microporosity. Both samples with EPS are slightly above the red line, which implies that the concentration of EPS does not have a significant influence on the peak microporosity. The samples processed with sawdust show the same behaviour: independent of

Table 5 Comparison of micro-CT-derived porosities, with those obtained from mercury intrusion and weighing

Sample characteristics	ϕ_{micro} (%) Equation (13)	ϕ_{macro} (%) Equation (1)	$\phi^{\text{CT}}_{\text{sample}}$ (%) Equation (14)	$\phi^{\text{Hg-intr}}_{\text{sample}}$ (%) Equation (17)	$\phi^{\text{weighing}}_{\text{sample}}$ (%) Equation (19)	err^{CT}(%) Equation (20)	$\text{err}^{\text{Hg-intr}}$(%) Equation (21)
10 (mass %) EPS; 880 °C	34.03	4.20	38.23	38.36	38.55	− 0.83	− 0.50
20 (mass %) EPS; 880 °C	34.76	6.90	41.66	36.41	42.16	− 1.19	− 13.65
10 (mass %) paper sludge; 880 °C	38.51	0	38.51	37.22	41.80	− 7.87	− 10.96
20 (mass %) paper sludge; 880 °C	41.24	0	41.24	42.08	42.76	− 3.54	− 1.58
40 (mass %) paper sludge; 880 °C	44.04	0	44.04	49.68	49.84	− 11.64	− 0.33
10 (mass %) sawdust; 880 °C	34.56	4.80	39.36	38.58	40.71	− 3.33	− 5.25
20 (mass %) sawdust; 880 °C	34.07	9.98	44.05	41.60	44.7	− 1.66	− 7.13
40 (mass %) sawdust; 880 °C	33.36	19.10	52.46	50.27	52.66	− 0.37	− 4.53
No agent; 880 °C clay	36.01	0	36.01	36.06	37.76	− 4.62	− 4.50
No agent; 1100 °C clay	28.83	0	28.83	28.49	28.21	2.22	0.98

the sawdust concentration, the microporosity stays nearly constant and close to the value of pure clay fired at 880 °C, see Table 4. In contrast, the microporosity of the samples processed with paper sludge increases with increasing concentration of the pore-forming agent, resulting in the overall voxel-related highest peak microporosity for 40% paper sludge, see Table 4. Similar results prevail for the overall microporosities ϕ_{micro} according to Eqs. (13) and (14), see Table 5. The overall microporosities per volume of ceramic sample, as a rule, comprise the by far major portion of the total porosity, namely between 60 and 100% of the latter, see Table 5. Finally, the total porosity derived from micro-CT agrees very well with that derived from mercury intrusion and weighing, with mercury intrusion porosimetry results being slightly worse than those stemming from weighing in combination with chemical analysis, see columns 7 and 8 of Table 5. In contrast to mercury intrusion porosimetry and weighing, our new CT evaluation scheme provides, through Eq. (11), detailed information on the microporosity distributions throughout the scanned ceramic samples, see Figs. 13 and 14. We reiterate from the "Materials and methods" section that we have introduced only one photon energy value as the basis for the quantitative intra-voxel evaluation, in spite of the use of a polychromatic CT device. Given the satisfactory results validated through independent experimental methods such as weighing and mercury intrusion, as shown in Table 5, we consider the aforementioned choice of only one energy value as a posteriori justified. At the same time, we emphasize that typical artefacts stemming from polychromatic light, such as streaks, dark bands, cupping, or flare artefacts [26–28], have been largely removed through the use of an aluminium filter with a thickness of 0.1 mm and Scanco's in-built beam hardening correction. This may lead to grey values of a quality "close to that" of synchrotron CT. Actually, the ability of

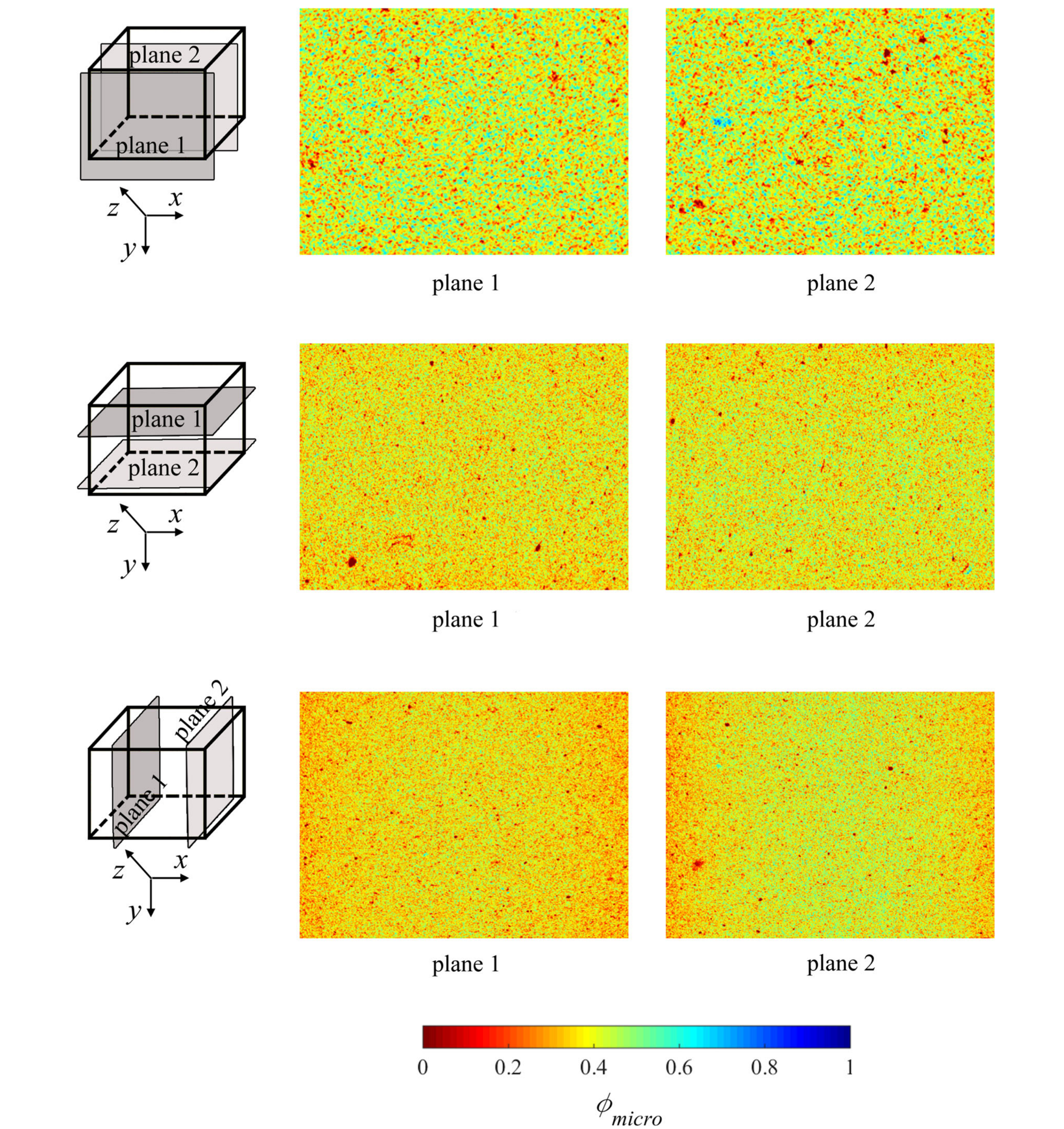

Figure 13 Distribution of microporosity ϕ_{micro} across different planes cut through the scanned sample without a pore-forming agent fired at 880 °C.

polychromatic systems to deliver results with a significant quantitative meaning has been explicitly shown in the context of bone density measurements, with errors not exceeding 10% [29–31]. Interestingly, this is fully consistent with the results of Table 5. Hence, it appears that low-cost X-ray microtomography systems, which undergo continuous improvement [32], do not only allow for precise reconstruction of geometrical features of several voxels size, but also allow for retrieving reliable

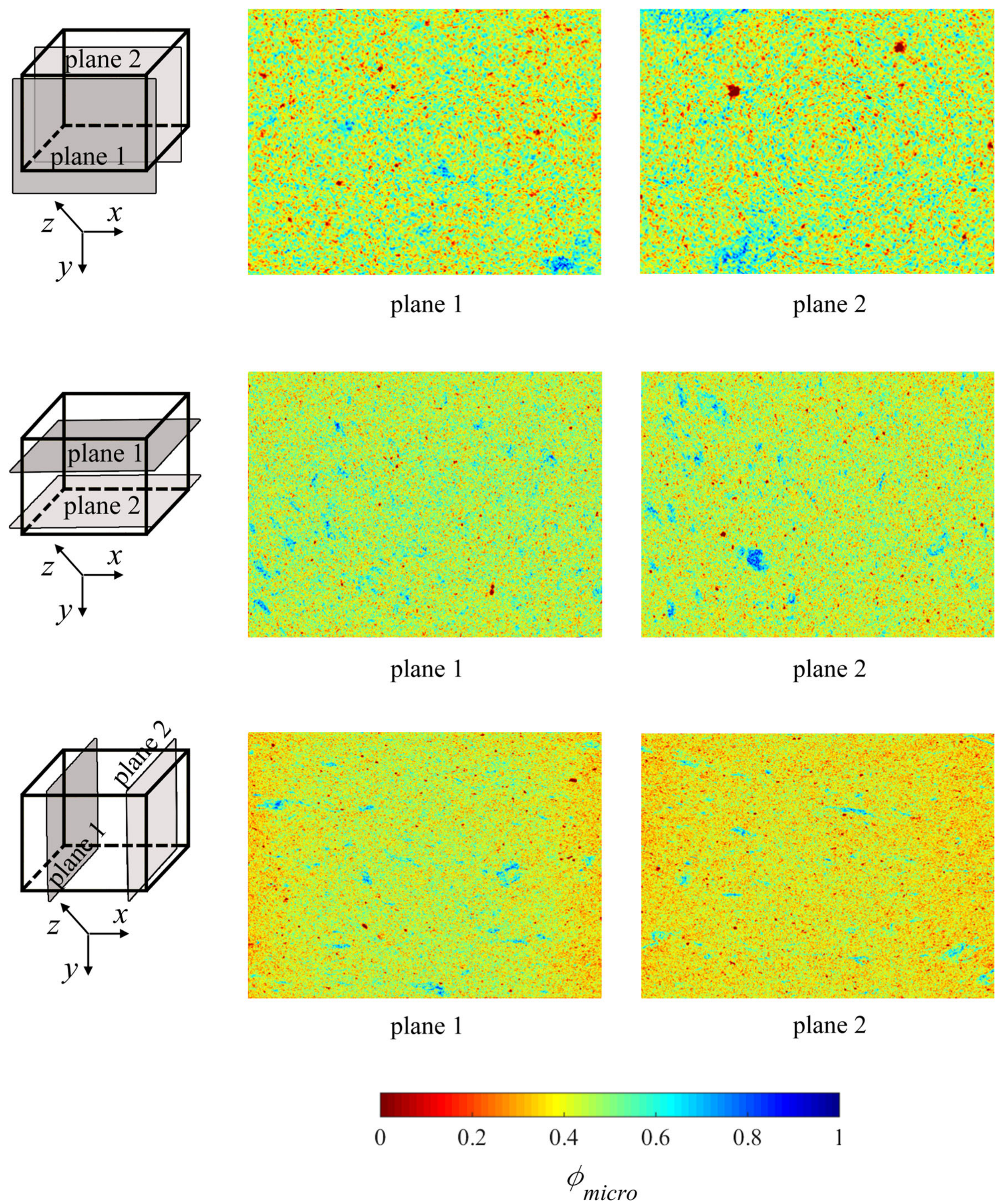

Figure 14 Distribution of microporosity ϕ_{micro} across different planes cut through the scanned sample processed with 20 (mass %) paper sludge fired at 880 °C.

quantitative information inside the voxels. The latter is valuable for a deeper multiscale analysis, which may, for example, focus on mechanical properties [33, 34].

Conclusion

Apart from the characteristics of the raw clay, the thermal and mechanical properties of bricks and clay blocks are governed by porosity, pore sizes, and pore morphologies. In this context, a new, validated, micro-CT evaluation technique reveals the following features:

- The pore size distribution depends critically upon the used pore-forming agent. EPS and sawdust induce macropores with sizes ranging from many micrometres up to millimetres, which paper sludge does not. Hence, paper sludge-processed ceramic samples only exhibit micropores of many nanometres to a few micrometres in size, such pores also contributing to the total porosity of EPS—and sawdust-processed ceramic samples.
- The macropores are larger and less numerous in the EPS as compared to the sawdust-processed samples, and the pores are typically elongated in shape and oriented towards the extrusion direction.
- The voxel-specific microporosity (measured per $6 \times 6 \times 6\,\mu m^3$ reference volume) depends strongly on the firing temperature and moderately on the sawdust and paper sludge content; which it is not affected by the EPS content.

Acknowledgements

Open access funding provided by TU Wien (TUW). The authors are thankful for the support by the 'Klima- und Energiefonds' through the programme 'Energie der Zukunft'. Funding for research was provided by Österreichische Forschungsförderungs-gesellschaft (Grant No. 843897).

Compliance with ethical standards

Conflict of interest All authors declare that they have no conflict of interest.

References

[1] García Ten J, Orts M, Saburit A, Silva G (2010) Thermal conductivity of traditional ceramics. Part I: influence of bulk density and firing temperature. Ceram Int 36(6):1951–1959

[2] García-Ten J, Orts M, Saburit A, Silva G (2010) Thermal conductivity of traditional ceramics: part II: influence of mineralogical composition. Ceram Int 36(7):2017–2024

[3] Bentz DP, Quenard DA, Kunzel HM, Baruchel J, Peyrin F, Martys NS, Garboczi EJ (2000) Microstructure and transport properties of porous building materials. II: three-dimensional X-ray tomographic studies. Mater Struct 33(3):147–153

[4] Hellmich C, Kober C, Erdmann B (2008) Micromechanics-based conversion of CT data into anisotropic elasticity tensors, applied to FE simulations of a mandible. Ann Biomed Eng 36(1):108–122

[5] Scheiner S, Sinibaldi R, Pichler B, Komlev V, Renghini C, Vitale-Brovarone C, Rustichelli F, Hellmich C (2009) Micromechanics of bone tissue-engineering scaffolds, based on resolution error-cleared computer tomography. Biomaterials 30(12):2411–2419

[6] Czenek A, Blanchard R, Dejaco A, Sigurjonsson OE, Örlygsson G, Gargiulo P, Hellmich C (2014) Quantitative intravoxel analysis of micro-CT-scanned resorbing ceramic biomaterials—perspectives for computer-aided biomaterial design. J Mater Res 29:2757–2772

[7] Prell D, Kyriakou Y, Kalender WA (2009) Comparison of ring artifact correction methods for flat-detector CT. Phys Med Biol 54(12):3881

[8] Sadi F, Lee SY, Hasan MK (2010) Removal of ring artifacts in computed tomographic imaging using iterative center weighted median filter. Comput Biol Med 40(1):109–118

[9] Kariem H, Pastrama MI, Roohani-Esfahani SI, Pivonka P, Zreiqat H, Hellmich C (2015) Micro-poro-elasticity of baghdadite-based bone tissue engineering scaffolds: a unifying approach based on ultrasonics, nanoindentation, and homogenization theory. Mater Sci Eng C 46:553–564

[10] Schneider CA, Rasband WS, Eliceiri KW (2012) NIH Image to ImageJ: 25 years of image analysis. Nat Methods 9(7):671–675

[11] Bolte S, Cordelieres FP (2006) A guided tour into subcellular colocalization analysis in light microscopy. J Microsc 224(3):213–232

[12] Doube M, Klosowski MM, Arganda-Carreras I, Cordelieres FP, Dougherty RP, Jackson JS, Schmid B, Hutchinson JR, Shefelbine SJ (2010) BoneJ: free and extensible bone image analysis in ImageJ. Bone 47(6):1076–1079

[13] Merkus HG (2009) Particle size measurements. No. 17 in particle technology series. Springer, Amsterdam

[14] Hubbell J (1982) Photon mass attenuation and energy-absorption coefficients. Appl Radiat Isot 33(11):1269–1290

[15] Seltzer S (1993) Calculation of photon mass energy-transfer and mass energy-absorption coefficients. Radiat Res 136(2):147–170

[16] Hubbell J, Seltzer S (2004) Tables of X-ray mass attenuation coefficients and mass energy-absorption coefficients from 1 keV to 20 MeV for elements $z = 1$ to 92 and 48 additional substances of dosimetric interest. https://www.nist.gov/pml/x-ray-mass-attenuation-coefficients. Accessed 7 Sept 2016

[17] Crawley EO, Evans WD, Owen GM (1988) A theoretical analysis of the accuracy of single-energy CT bone-mineral measurements. Phys Med Biol 33(10):1113–1127

[18] Jackson DF, Hawkes D (1981) X-ray attenuation coefficients of elements and mixtures. Phys Rep 70(3):169–233

[19] Hubbell J (1977) Photon mass attenuation and mass energy-absorption coefficients for H, C, N, O, Ar, and seven mixtures from 0.1 keV to 20 MeV. Radiat Res 70:58–81

[20] Halliday D, Resnick R, Walker J (2010) Fundamentals of physics. Wiley, London

[21] Prinz H, Strauss R (2011) Ingenieurgeologie, 5th edn. Springer Spektrum, Berlin

[22] Birch F (1960) The velocity of compressional waves in rocks to 10 kilobars: 1. J Geophys Res 65(4):1083–1102

[23] Birch F (1961) The velocity of compressional waves in rocks to 10 kilobars: 2. J Geophys Res 66(7):2199–2224

[24] Giesche H (2006) Mercury porosimetry: a general (practical) overview. Part Part Syst Charact 23(1):9–19

[25] POROTEC (2001) Mercury porosimetry—pascal 140 240 440 manual. Porotec GmbH

[26] Duerinckx AJ, Macovski A (1978) Polychromatic streak artifacts in computed tomography images. J Comput Assist Tomogr 2(4):481–487

[27] Joseph PM, Spital RD (1978) A method for correcting bone induced artifacts in computed tomography scanners. J Comput Assist Tomogr 2(1):100–108

[28] Schulze R, Berndt D, D'Hoedt B (2010) On cone-beam computed tomography artifacts induced by titanium implants. Clin Oral Implants Res 21(1):100–107

[29] Mulder L, Koolstra JH, Eijden TMGJV (2004) Accuracy of micro-CT in the quantitative determination of the degree and distribution of mineralization in developing bone. Acta Radiol 45(7):769–777

[30] Zou W, Hunter N, Swain M (2011) Application of polychromatic μ CT for mineral density determination. J Dent Res 90(1):18–30

[31] Davis G, Evershed A, Elliott J, Mills D (2010) Quantitative X-ray microtomography with a conventional source. In: Developments in X-ray tomography VII, vol 7804

[32] Vilar A, dos Santos T, Machado A, Oliveira D, Azeredo S, Lopes R (2017) X-ray microtomography system for small and light samples using a flat panel detector. Rev Sci Instrum 88(10):105112

[33] Blanchard R, Dejaco A, Bongaers E, Hellmich C (2013) Intravoxel bone micromechanics for micro-CT-based finite element simulations. J Biomech 46(15):2710–2721

[34] Dejaco A, Komlev VS, Jaroszewicz J, Swieszkowski W, Hellmich C (2016) Fracture safety of double-porous hydroxyapatite biomaterials. Bioinspir Biomim Nan 5(1):24–36